

# 1 Magnitude Scales for Marsquakes Calibrated from InSight Data

2 Böse, M.\*; S. Stähler, N. Deichmann, D. Giardini, J. Clinton, P. Lognonné, S. Ceylan, M. van Driel, C.  
3 Charalambous, N. Dahmen, A. Horleston, T. Kawamura, A. Khan, M. Knapmeyer, G. Orhand-  
4 Mainsant, J.-R. Scholz, F. Euchner, B.W. Banerdt

5

6 \*Corresponding author: Maren Böse, [maren.boese@sed.ethz.ch](mailto:maren.boese@sed.ethz.ch), Institute of Geophysics, ETH  
7 Zurich, Sonneggstrasse 5, 8092 Zurich, Switzerland

8 **The authors acknowledge there are no conflicts of interest recorded.**

9

## 10 ABSTRACT

11 In preparation for the NASA InSight (Interior exploration using Seismic Investigations, Geodesy  
12 and Heat Transport) Discovery Program mission, Böse *et al.* (2018) calibrated magnitude scales  
13 for marsquakes that incorporated the pre-launch knowledge on Mars' interior structure and the  
14 expected ambient and instrumental noise. Now, using data collected during the first two years  
15 after the successful deployment of the InSight very-broadband seismometer on the Martian  
16 surface, we revise these relations to account for the seismic and noise characteristics observed on  
17 Mars. The data collected so far (until October 12, 2020) includes 485 seismic event detections and  
18 suggest that (1) marsquakes are characterized by energy between  $\sim 0.1$  and 10 Hz; (2) though first  
19 arriving P- and S-wave phases are regularly identified and assigned, both surface-waves and  
20 secondary phase arrivals are extremely challenging to identify; (3) the majority of identified events  
21 include a strong excitation of an unexpected 2.4 Hz ground resonance; and (4) so-called high-  
22 frequency events exist that are visible mainly as guided  $P_g/S_g$  wave trains. In view of these  
23 observations, we update our scaling relations for the spectral and body-wave magnitudes,  $M_{W,spec}^{Ma}$ ,  
24  $m_b^{Ma}$  and  $m_{bS}^{Ma}$ , and introduce a new magnitude scale,  $M_{2.4}^{Ma}$ , for high-frequency events. We use these  
25 scales to determine that the magnitudes of events in the current InSight v.5 catalog range between  
26 1.1 and 3.7, with event-specific uncertainties  $\sigma_M$  ranging from 0.2 to 0.5. Due to the currently  
27 unclear interpretation of high-frequency events, magnitude estimates for these events primarily  
28 serve for a relative comparison.

29

## 30 INTRODUCTION

31 The NASA InSight (Interior exploration using Seismic Investigations, Geodesy and Heat Transport)  
32 Discovery Program mission successfully launched on May 5, 2018, from Vandenberg Air Force  
33 Base, California, and landed on Mars about six months later (Banerdt *et al.*, 2020). The deployment  
34 of the three-component ultra-sensitive very-broadband (VBB) seismometer (Lognonné *et al.*,  
35 2019; 2020) was completed by the end of February 2019 (Giardini *et al.*, 2020). Since then, the  
36 Marsquake Service (MQS), as part of the InSight Science Team, routinely inspects manually the  
37 continuous 20 samples-per-second (sps) seismic data returned by InSight (Clinton *et al.*, 2018).  
38 Event data at higher sampling (100 sps) is recovered whenever possible. (The available bandwidth  
39 depends on multiple factors related to satellites around Mars that relay the data, as well as  
40 competing data volumes from other Martian missions and even other instruments operating on  
41 InSight.) Until October 12, 2020 (first Martian year of the InSight mission), MQS has identified 485  
42 seismic events that have been interpreted as marsquakes (InSight Marsquake Service, 2021). All  
43 of these events are characterized by energy between  $\sim 0.1 - 10$  Hz and have durations typically  
44 ranging from 5 - 30 minutes. A small number of events include energy of up to 35 Hz. Waveform  
45 amplitudes typically rise only slightly above the lowest background noise, and this lowest noise  
46 typically occurs only for a few hours per sol (a Martian sol is 24h 39.5' long). A detailed description  
47 of the event catalog and general characteristics of the data collected so far are given in Clinton *et al.*  
48 (2020), Giardini *et al.* (2020), and Ceylan *et al.* (2020); noise and event amplitudes are discussed  
49 in Charalambous *et al.* (2021).

50  
51 The seismic events identified in the InSight MQS catalog fall into two families (Clinton *et al.*, 2020).  
52 A low-frequency family, which is similar to terrestrial earthquakes, comprises events with clearly  
53 defined P- and S-wave arrivals, even though they may have low signal-to-noise ratios (SNR). A  
54 second family of high-frequency events is characterized by long-duration wave trains, similar to  
55 guided Po/So waves in the oceanic crust (Kennett & Furumura, 2013). The MQS further divides  
56 the two events families into the following five classes:

- 57 • Low-frequency family:
  - 58 ○ *low-frequency (LF)* events have energy on all 3 components below 2.4 Hz;
  - 59 ○ *broadband (BB)* events have energy on 3 components, predominantly below 2.4 Hz, but

- 60 also including excitement at and possibly also above 2.4 Hz;
- 61 • High-frequency family:
- 62 ○ *high-frequency (HF)* events have energy on 3 components, predominantly at 2.4 Hz and
- 63 above;
- 64 ○ *very high-frequency (VF)* events are a special case of *HF* events with energy on the
- 65 horizontal components at higher frequencies being significantly larger than on the
- 66 vertical;
- 67 ○ *2.4Hz resonance (2.4Hz)* events have energy on 3 components, centered around 2.4 Hz
- 68 (ambient) resonance with very limited excitation above or below (likely small amplitude
- 69 *HF* events).

70

71 An additional class of signals, *super-high frequency (SF)* events, are also included in the MQS

72 catalog. These events have an order of magnitude shorter durations than the other events and only

73 include energy above 5 Hz. They are considered to be associated with a very local source (Dahmen

74 *et al.*, 2021), but further research is needed to provide a stable interpretation of these signals. *SF*

75 events are not considered further in this study.

76

77 The InSight catalog v.5 (until 2020/10/12; sol 668) holds a total of 279 seismic events with

78 distance estimates of any kind (and an additional 206 events without distance estimates or of

79 unclear origin), including 20 *LF* ( $20^\circ \leq \Delta \leq 100^\circ$ ), 9 *BB* ( $25^\circ < \Delta < 90^\circ$ ), 50 *HF* ( $20^\circ < \Delta < 30^\circ$ ), 21 *VF*

80 ( $3^\circ < \Delta < 30^\circ$ ), and 179 *2.4Hz* ( $6^\circ < \Delta < 40^\circ$ ) events (Table 1). The *2.4Hz* events are likely weak

81 examples of *HF* events that would not be observable, but for the additional excitation of the 2.4 Hz

82 subsurface resonance rising above the background noise (Clinton *et al.*, 2020). *VF* events are *HF*

83 events with clear differences in energy between horizontal and vertical components and a rising

84 displacement spectrum on the horizontal components. Following Giardini *et al.* (2020) and van

85 Driel *et al.* (2021), our current understanding is that the seismic waveforms of events in the high-

86 frequency (*HF*, *VF*, *2.4Hz*) family are dominated by guided crustal waves in a shallow layer. This

87 could be a regional sediment layer, or in the most extreme case, the whole crust and lithosphere,

88 as observed in the oceanic crust on Earth (Kennett & Furumura, 2013). The assumed propagation

89 path of seismic waves in the two event families is illustrated in Figure 1.

90

91 The MQS assigns event quality according to the following conventions: (1) High-quality events ('A')  
92 show multiple clear and identifiable phases and clear polarisation (i.e. they can be located using  
93 the probabilistic approach of Böse *et al.*, 2016); (2) medium quality events ('B') show multiple clear  
94 and identifiable phases, but no polarisation (i.e. only their distance from the lander can be  
95 determined, but no absolute location); (3) low-quality events ('C') show no clear phases, but  
96 signals are clearly observed; and (4) suspicious events ('D') show only weakly observed signals or  
97 signals that may not be attributable to a seismic event. In addition to this quality scheme, all events  
98 are characterized by an SNR measurement (Giardini *et al.*, 2020; Charalambous *et al.*, 2021).

99

100 In the v.5 MQS catalog, distance estimates are available for all quality 'A' and 'B' events, and for the  
101 majority of quality 'C' and some quality 'D' events. A complete description of the approach is given  
102 in Clinton *et al.* (2020) and is summarized below. For low-frequency family events the  
103 methodology follows Böse *et al.* (2016). Using large sets of travel time tables derived from a priori  
104 velocity models, distances are computed using picks identified in either the time or spectral  
105 domain that are interpreted as P- and S- phases. This allowed to constrain 15 of the 43 low-  
106 frequency family events in distance. Further work using alignment of waveform envelopes allows  
107 these distances to be refined and additional events that do not have clear onsets to be assigned  
108 distances (see Giardini *et al.*, 2020). In this manner, 27 of the 43 (63%) low-frequency family  
109 events in the MQS catalog are assigned distances. In cases where there are differences between  
110 distances based on phase picks and alignments, the alignment-based distances are preferred. For  
111 events in the high-frequency family, picks are typically identified using a STA-LTA filter targeting  
112 the 2.4 Hz resonance. Two phase onsets are normally visible, that are interpreted as  $P_g$  and  $S_g$ . Since  
113 the propagation velocities of those are not known, we cannot confidently determine absolute  
114 distances. In order to provide an approximate distance, as well as a robust estimate of the relative  
115 distances within the high-frequency family, we assume that  $P_g$  propagates with  $v_p = 4$  km/s and  $S_g$   
116 with  $v_s = v_p / \sqrt{3} = 2.3$  km/s. For 249 of 441 (56%) high-frequency family events in the MQS catalog,  
117  $P_g$  and  $S_g$  phases are both identified and we could assign distances this way.

118

## 119 **Pre-Launch Magnitude Calibrations**

120 Assigning event magnitudes is an important part of characterizing seismicity. In our pre-launch  
121 paper (Böse *et al.*, 2018) we had calibrated magnitude scales for marsquakes by simulating the  
122 seismic wave propagation through a set of hypothetical 1D Mars models, that incorporated the  
123 pre-mission knowledge on Mars interior structure (Smrekar *et al.*, 2019) and the assumed ambient  
124 and instrumental noise (Murdoch *et al.*, 2015; Mimoun *et al.*, 2017), using the spectral element  
125 solver AxiSEM (Nissen-Meyer *et al.*, 2014; van Driel *et al.*, 2017). Inspired by relations developed  
126 for Earth, we had defined six magnitude scales: local Mars magnitude,  $M_L^{\text{Ma}}$ ; P- and S-wave  
127 magnitudes,  $m_b^{\text{Ma}}$  and  $m_{bS}^{\text{Ma}}$ , at a period of 3 s; surface-wave magnitude,  $M_S^{\text{Ma}}$ ; and spectral  
128 magnitudes,  $M_{\text{FB}}^{\text{Ma}}$  and  $M_{\text{F}}^{\text{Ma}}$ . We had calibrated these scales relative to the seismic moment  
129 magnitude at  $M_W = 5.5$  by correcting filtered phase or spectral amplitudes in the simulated  
130 waveforms for distance-dependent attenuation using

131

$$132 \quad M_i^{\text{Ma}} = \log_{10}(A_i) + a_i \log_{10}(\Delta) + c_i \quad (1)$$

133

134 The superscript “Ma” stands for “Mars” (following BSSA accepted standard for planetary  
135 magnitude in accordance with IAU practice);  $a_i$  and  $c_i$  are scaling coefficients for the different  
136 magnitude types;  $A_i$  is a measure of amplitude that is also dependent on magnitude type – and can  
137 be the filtered peak displacement amplitude [ $m$ ] determined from the waveform time-series  
138 within a certain time-window, or the spectral amplitude [ $m/\sqrt{\text{Hz}}$ ] determined from the square-  
139 root of the long-period plateau of the power spectral density (PSD) of the displacement;  $\Delta$  is the  
140 epicentral distance in degrees [ $^\circ$ ]. For both the local and the surface-wave based magnitude scales,  
141 Böse *et al.* (2018) included an additional term for source depth. In a second regression, Böse *et al.*  
142 (2018) had calibrated the six scales with the known seismic moment,  $M_0$ , of the simulations across  
143 the entire magnitude range  $1.0 \leq M_W \leq 7.0$  to obtain a conversion relation to moment magnitude  
144  $M_W$ .

145

146 The InSight data collected so far suggest that (1) two families of marsquakes exist (low-frequency  
147 and high-frequency; see above), which need separate magnitude scales, (2) the frequency content  
148 of the more classic low-frequency events ranges from 0.1 to 1 Hz, the high-frequency events from

149 1.5 to up to 10 (and possibly larger) Hz, (3) though first arriving P- and S-wave phases are regularly  
150 identified and assigned, both surface-waves and secondary phase arrivals are extremely  
151 challenging to identify and cannot be used for regular analysis, and (4) many high-frequency  
152 events are primarily visible as an enhanced excitation of the natural 2.4 Hz ambient mode, which  
153 is believed to originate from the substructure below the lander (Ceylan *et al.*, 2020; Dahmen,  
154 Zenhäuser *et al.*, *subm.*). In view of these observations, we update our scaling relations (Böse *et al.*,  
155 2018) for the body-wave magnitudes,  $m_b^{\text{Ma}}$  and  $m_{bS}^{\text{Ma}}$ , and introduce a new magnitude scale,  $M_{2.4}^{\text{Ma}}$ ,  
156 specifically, for high-frequency events. The surface-wave magnitude,  $M_S^{\text{Ma}}$ , is not updated, given  
157 the lack of clear surface-wave observations (which is likely due to the small sizes of marsquakes  
158 detected so far; Clinton *et al.*, 2020), and as explained in the following section, we replace the  
159 spectral magnitude  $M_{\text{FB}}^{\text{Ma}}$  introduced in Böse *et al.* (2018) by  $M_{W,\text{spec}}^{\text{Ma}}$ .

160

161

## 162 **METHOD**

163 Based on the data in the InSight v.5 event catalog (until 2020/10/12; InSight Marsquake Service,  
164 2021) and formulations of Böse *et al.* (2018), we calibrate in this study four magnitude scales:  
165 spectral magnitude,  $M_{W,\text{spec}}^{\text{Ma}}$  (computed over the full body-wave train), time-domain P- and S-  
166 body-wave magnitudes,  $m_b^{\text{Ma}}$  and  $m_{bS}^{\text{Ma}}$ , and 2.4 Hz magnitude,  $M_{2.4}^{\text{Ma}}$ . We will describe each scale in  
167 detail in the following subsections. The MQS tracks and internally catalogs the corresponding  
168 amplitudes (they are given in Table S1 in the Electronic Supplement of this article): spectral  
169 plateau amplitude,  $A_0$ , for low- and high-frequency events (excluding the majority of *VF* events that  
170 often have unclear  $A_0$  and all *2.4Hz*); time domain body-wave amplitudes,  $A_P$  and  $A_S$ , at 0.2 - 0.5  
171 Hz for low-frequency events (*LF*, *BB*); and 2.4 Hz spectral and time domain amplitudes,  $A_{2.4,\text{spec}}$  and  
172  $A_{2.4,\text{pick}}$ , for high-frequency events (*HF*, *VF*, *2.4Hz*). Examples of each type are shown in Figure 2.

173

174 Unlike in Böse *et al.* (2018), we calibrate each magnitude directly against the moment magnitude,  
175  $M_W$ , which is possible for the limited magnitude range ( $< 4$ ) that we work in. We adopt the  
176 definition of moment magnitude,  $M_W$ , for Earth, which is based on the seismic moment,  $M_0$  [in MKS  
177 units] (Hanks and Kanamori, 1979):

178

179 
$$M_W = \frac{2}{3} (\log_{10}(M_0) - 9.1) \quad (2a)$$

180

181 Assuming that the far-field displacement,  $\mathbf{u}(\mathbf{x}, \tau)$ , due to the direct S-wave from the source to the  
182 receiver is a unipolar pulse and that  $M_0$  is proportional to the area under this pulse, it follows (e.g.  
183 Aki & Richards, 1980)

184

185 
$$M_0 = \frac{4\pi\rho v_s^3}{R_S^{\theta\phi} S_f} R \int_0^T \mathbf{u}(\mathbf{x}, \tau) d\tau = c_0 R \Omega_0 \quad (2b)$$

186

187 with average radiation pattern  $R_S^{\theta\phi}$ , free-surface amplification  $S_f$ , hypocentral distance  $R$ , density  
188  $\rho$ , shear-wave velocity  $v_s$  at the source, and spectral displacement amplitude-density  $\Omega_0 =$   
189  $\int_0^T \mathbf{u}(\mathbf{x}, \tau) d\tau$  at frequency 0. Inserting equation (2b) in (2a) gives

190

191 
$$M_w = \frac{2}{3} (\log_{10}\Omega_0 + 1.0 \log_{10}R + \log_{10}c_0 - 9.1) \quad (2c)$$

192

193 To describe the spectral magnitude on Mars, we adopt in this study a more general form

194

195 
$$M_{W,\text{spec}}^{\text{Ma}} = \frac{2}{3} (\log_{10}A_0 + a_i \log_{10}\Delta + c_i) \quad (3a)$$

196

197 where  $A_0$  [ $m/\sqrt{\text{Hz}}$ ] is the square-root of the spectral amplitude extrapolated from the long-period  
198 plateau of the event power spectral density (PSD) displacement spectrum. As a consequence of the  
199 relation between amplitude spectral density and power spectral density, it is  $\Omega_0 = A_0/\sqrt{T}$ , where  
200  $T$  is the length of the data window used in the computation of the PSD. We replaced in equation  
201 (3a) the hypocentral  $R$  [ $m$ ] by the epicentral distance  $\Delta$  [ $^\circ$ ], assuming that the seismic ray paths  
202 have a curvature similar to the curvature of the Martian surface. In equation (3a),  $\log_{10}(\sqrt{T})$  as

203 well as the logarithm of the conversion factor between meters and degrees are included in the  
204 additive coefficient  $c_i$ .

205

206 In this study,  $M_{W,spec}^{Ma}$  is set as a reference for the calibration of the other magnitude scales for  
207 events with measurements of multiple amplitude types (Figure 3). This is because (1) we consider  
208 the  $M_{W,spec}^{Ma}$  the most reliable measurement of the seismic moment,  $M_0$ , and thus  $M_W$ , because it is  
209 estimated from the extrapolated spectrum at long periods (20 - 100 s), thus mitigating the effect  
210 of attenuation; (2) due to the low SNR of many events, the picking of peak amplitudes in the time  
211 domain is less robust compared to the calculation of a spectrum of a long time window, considering  
212 the duration of these events generally range from 5 - 30 minutes (Figure 2); and (3) aside from the  
213 majority of *VF* and all *2.4Hz* resonance events,  $M_{W,spec}^{Ma}$  can be determined for all low- and high-  
214 frequency events in the InSight MQS catalog (Table 1 & Figure 3).

215

216 In order to derive magnitude scales that approximate  $M_W$  and that can be applied to quantify the  
217 source sizes of all events in the InSight catalog regardless of their frequency content, we will start  
218 this work with an absolute calibration of  $M_{W,spec}^{Ma}$  (strictly speaking of  $M_{W,spec,LF}^{Ma}$  for low-  
219 frequency and of  $M_{W,spec,HF}^{Ma}$  for high-frequency events) relative to  $M_W$ , based on synthetic data and  
220 theoretical considerations, respectively. Then, in the next step, we use the low-frequency events  
221 (*LF*, *BB*) in the InSight catalog to calibrate body-wave magnitudes,  $m_b^{Ma}$  and  $m_{bS}^{Ma}$ , relative to  
222  $M_{W,spec,LF}^{Ma}$ , and the high-frequency events (*HF*) to calibrate the 2.4 Hz magnitude,  $M_{2.4}^{Ma}$ , relative to  
223  $M_{W,spec,HF}^{Ma}$  (Figure 3). The resulting  $M_{2.4}^{Ma}$  scale can be applied also to the *VF* and *2.4Hz* events to  
224 obtain magnitude estimates that are comparable to the other events in the InSight catalog, and  
225 hence ensure that every marsquake with an assigned distance also has a magnitude.

226

227 Our magnitude calibration is done by regressing the InSight data to determine the coefficients  $a_i$   
228 and  $c_i$  in equation (1). This equation predicts a power decay of seismic amplitudes, i.e. a constant  
229  $a_i$  factor for all magnitudes and distances. This assumption, however, is valid only for events  
230 outside the low (S-wave) amplitude-zone between  $35^\circ$  and  $60^\circ$  (e.g. Giardini *et al.*, 2020).  
231 Therefore, we use only S-wave amplitudes for events outside this zone for magnitude calibration



232 of  $m_{bS}^{\text{Ma}}$ .

233

### 234 **Absolute Calibration of Spectral Magnitude $M_{W,\text{spec}}^{\text{Ma}}$**

235 We start with an absolute calibration of spectral magnitude  $M_{W,\text{spec}}^{\text{Ma}}$  (strictly speaking of  $M_{W,\text{spec},\text{LF}}^{\text{Ma}}$

236 and  $M_{W,\text{spec},\text{HF}}^{\text{Ma}}$ ) with  $M_W$  adopting the functional form in equation (3a). The spectral magnitude

237 can be computed for all low- and high-frequency events, excluding *VFs* that have unclear  $A_0$  and all

238  $2.4\text{Hz}$  events, in the InSight event catalog (Figure 3) using their spectral amplitude,  $A_0$  (Figure 2).

239 The corresponding spectra are computed from the instrument-corrected displacement waveforms

240 that have been rotated into ZNE (up-down, north-south, east-west) components, from which the

241 linear trend has been removed. We apply Welch's power spectral density (PSD) method to 25.6 s

242 long Hanning-windowed time segments with 50% overlap and with zero-padding to 4096 samples

243 (102.4 s), and then compute the square-root of the resulting spectrum. From the amplitude and

244 slope between 0.1 and 0.8 Hz, the low-frequency plateau of the spectrum is extrapolated.

245

246 To determine the spectral amplitude,  $A_0$  [ $m/\sqrt{\text{Hz}}$ ], we fit the following function to the spectra

247 (vertical component)

248

$$249 \quad A(f) = A_0 A_{\text{src}}(f) A_{\text{att}}(f) \quad (4a)$$

250

251 which combines a simple source spectrum (Brune, 1970)

252

$$253 \quad A_{\text{src}}(f) = \frac{1}{1+(f/f_c)^2} \quad (4b)$$

254

255 with corner frequency  $f_c$  with an exponential attenuation term described by

256

$$257 \quad A_{\text{att}}(f) = \exp(-\pi f t^*) \quad (4c)$$

258

259 where  $t^*$  describes the energy loss at high frequencies due to attenuation. Assuming that the  
260 corner frequency is related to the stress drop,  $f_c = 0.49 v_s (\Delta\sigma/M_0)^{1/3}$ , a shear-wave velocity of  $v_s$   
261 = 3.5 km/s in the source region, and a stress drop of  $\Delta\sigma = 1.0$  MPa, the predicted corner frequency  
262 of the source-time function is above 1 Hz and therefore the observed spectrum between 0.1 and 1  
263 Hz is dominated by attenuation effects. We therefore fix  $f_c$  at a value of 1 Hz, so that  $A_0$  and  $t^*$  can  
264 be inferred by linear inversion. For the high-frequency events, in contrast, we invert for all three  
265 parameters ( $A_0$ ,  $t^*$ , and  $f_c$ ).  $t^*$  ranges from 0.6 - 4.3 s for the observed low-frequency and from 0.05  
266 - 0.5 s for the observed high-frequency events (see Table S1 in Electronic Supplements). Detailed  
267 subsurface structural models below the InSight lander are currently being developed (e.g.  
268 Lognonné *et al.*, 2020) and will help to fine-tune these parameters in the future (see Conclusions  
269 & Outlook).

270

### 271 ***Spectral Magnitude $M_{W,spec,LF}^{Ma}$ for Low-Frequency Events***

272 With the current interpretation that seismic waves of marsquakes in the low-frequency event  
273 family have travelled through the Martian lithosphere and mantle (see Introduction; Figure 1), we  
274 assume a volumetric seismic wave propagation for these events. By the conservation of energy,  
275 standard geometrical spreading of seismic wave amplitudes predicts that the energy in a unit area  
276 of the growing wavefront decreases as  $\Delta^2$ . Body-wave amplitudes hence decay with  $\Delta^{-1}$ , so we  
277 expect  $\log_{10}(A_0)$  to decrease by about one unit per unit change in  $\log_{10}(\Delta)$ , corresponding to  $a_i \approx$   
278 1.0 (see equation 2c). Therefore, we model the decay of seismic wave amplitudes with distance  
279 for the low-frequency events equation (3a) as  $a_i = (1.0 \pm 0.1)$ , assuming an uncertainty of 0.1 due  
280 to leaking energy and effects of the velocity structure on geometrical spreading.

281

282 In order to determine the constant  $c_i$  in equation (3a) for the low-frequency events, we model a  
283 set of several hundreds of synthetic marsquakes at  $\Delta = 5^\circ - 150^\circ$  distance and down to 50 km  
284 depth for different  $M_0$  and source mechanisms using Instaseis (van Driel *et al.*, 2015; Ceylan *et al.*,  
285 2017) for a set of representative Mars models described in Clinton *et al.* (2017) for the time-

286 window before surface-wave arrival. The same set of models and seismic propagation code was  
 287 used in our original pre-launch magnitude paper (Böse *et al.*, 2018). From these simulations we  
 288 determine  $c_i = (12.6 \pm 0.5)$ , and thus we obtain for the spectral magnitude for low-frequency  
 289 events (*LF, BB*)

$$291 \quad M_{W,\text{spec},LF}^{\text{Ma}} = \frac{2}{3} (\log_{10}(A_0) + (1.0 \pm 0.1) \log_{10}(\Delta) + (12.6 \pm 0.5)) \quad (5a)$$

292  
 293 The coefficients in equation (5a) differ from those in Böse *et al.* (2018), since here  $a_i$  has been set  
 294 to 1.0.

295  
 296 The spectral fitting procedure to determine  $A_0$  (equation (4a)) and thus  $M_{W,\text{spec},LF}^{\text{Ma}}$  (equation (5a))  
 297 is affected by uncertainties, which can be used to estimate magnitude errors  $\sigma_{M_{W,\text{spec},LF}^{\text{Ma}}}^2$ . It follows  
 298 from error propagation

$$299$$

$$300 \quad \sigma_M^2 = \sigma_{M_{W,\text{spec},LF}^{\text{Ma}}}^2 = \left(\frac{2}{3}\right)^2 \left[ \left| \frac{\partial M_{W,\text{spec},LF}^{\text{Ma}}}{\partial \log_{10}(A_0)} \right|^2 \sigma_{\log_{10}(A_0)}^2 \right.$$

$$301 \quad \left. + \log_{10}(\Delta)^2 \left| \frac{\partial M_{W,\text{spec},LF}^{\text{Ma}}}{\partial a_i} \right|^2 \sigma_{a_i}^2 + a_i^2 \left| \frac{\partial M_{W,\text{spec},LF}^{\text{Ma}}}{\partial \log_{10}(\Delta)} \right|^2 \sigma_{\log_{10}(\Delta)}^2 \right.$$

$$302 \quad \left. + \left| \frac{\partial M_{W,\text{spec},LF}^{\text{Ma}}}{\partial c_i} \right|^2 \sigma_{c_i}^2 \right]$$

$$303 \quad = \frac{4}{9} (\sigma_{\log_{10}(A_0)}^2 + 0.1 \log_{10}(\Delta)^2 + \sigma_{\log_{10}(\Delta)}^2 + 0.3)$$

$$304 \quad = 0.44 \sigma_{\log_{10}(A_0)}^2 + 0.044 \log_{10}(\Delta)^2 + 0.44 \sigma_{\log_{10}(\Delta)}^2 + 0.13 \quad (5b)$$

305  
 306 We determine  $\sigma_{\log_{10}(A_0)}$  from the uncertainty (standard deviation) in spectral fitting for each low-  
 307 frequency event individually. The second term,  $0.044 \log_{10}(\Delta)^2$ , suggests a distance-dependent  
 308 error, ranging between 0.074 at  $\Delta = 20^\circ$  and 0.17 at  $\Delta = 90^\circ$  and that is 0.1 at  $\Delta = 32^\circ$ .  $\sigma_{\log_{10}(\Delta)}$  is  
 309 more difficult to determine. We use distance uncertainties as provided in the InSight catalog v.5  
 310 whenever available. For events without uncertainty estimates we assume a distance error of 25%  
 311 (see Discussion). The resulting magnitude uncertainties are provided in Table S1.

312

313

314 **Spectral Magnitude  $M_{W,\text{spec},HF}^{\text{Ma}}$  for High-Frequency Events**

315 With the current interpretation that seismic waves of high-frequency events are guided waves  
316 travelling in the crust or in a shallow layer (see Introduction; Figure 1), we assume a surface-wave  
317 propagation for these events. The attenuation of surface-waves is generally more complex than  
318 that of body-waves. Based on values determined by Evernden *et al.* (1971), Basham (1971), and  
319 Nuttli (1973) for short-period Lg and Rg phases on Earth (see also Bormann *et al.*, 2013), we set  
320 in equation (3a)  $a_i = (0.8 \pm 0.1)$  for the high-frequency events. Assuming that the spectral  
321 amplitudes at close distance to the seismic source (here: at  $\Delta = 1^\circ$ ) are similar for both low- and  
322 high-frequency events, we determine from equation (5a)  $c_i = 12.8$ , and thus obtain for the  
323 spectral magnitudes for high-frequency events (*HF* and *VF*)

324

325 
$$M_{W,\text{spec},HF}^{\text{Ma}} = \frac{2}{3} (\log_{10}(A_0) + (0.8 \pm 0.1) \log_{10}(\Delta) + 12.8) \quad (5c)$$

326

327 For simplicity, we set here  $\sigma_{M_{W,\text{spec},HF}^{\text{Ma}}} = 0.2$  for all high-frequency events, pointing out, however,  
328 that the true uncertainties, in particular considering the uncertainty in the distance estimate, could  
329 be much larger.

330

331 **Calibration of Body-wave Magnitudes  $m_b^{\text{Ma}}$  and  $m_{bS}^{\text{Ma}}$  Relative to  $M_{W,\text{spec}}^{\text{Ma}}$**

332 In the next step, we calibrate P- and S-body-wave magnitudes,  $m_b^{\text{Ma}}$  and  $m_{bS}^{\text{Ma}}$ . These magnitudes  
333 can be determined for low-frequency events (*LF*, *BB*), excluding for  $m_{bS}^{\text{Ma}}$  the events S0325a, S0357a,  
334 S0183a, and S0205a that fall into the low (S-wave) amplitude-zone (Giardini *et al.*, 2020) (Table 1  
335 & Figure 3). We compute  $m_b^{\text{Ma}}$  and  $m_{bS}^{\text{Ma}}$  from the peak displacement amplitudes  $A_p$  and  $A_s$ , which  
336 we determine from the integrated and filtered velocity waveforms (applying a 6<sup>th</sup> order causal  
337 Butterworth bandpass with corner frequencies of 0.167 Hz and 0.5 Hz) in the time window of the  
338 compression- or shear-wave arrivals, respectively (Figure 2b). We use the vertical component of

339 the seismograms to compute  $A_P$  and the maximum of the two horizontal components to compute  
340  $A_S$ .

341

342 From the SNR-weighted amplitude regression of  $A_P$  and  $A_S$  with  $M_{W,spec,LF}^{Ma}$ , we find for the P-wave  
343 magnitudes

344

$$345 \quad m_b^{Ma} = \log_{10}(A_P) + 0.73 \log_{10}(\Delta) + 11.8 \quad (6)$$

346

347 and for S-wave magnitudes

348

$$349 \quad m_{bS}^{Ma} = \log_{10}(A_S) + 1.06 \log_{10}(\Delta) + 10.9 \quad (7)$$

350

351 The MQS assigns SNRs to each (time-domain) picked amplitude (Clinton *et al.*, 2020). Only the low-  
352 frequency event family (*LF* and *BB*) have significant energy between 0.2 and 0.5 Hz, so  $m_b^{Ma}$  and  
353  $m_{bS}^{Ma}$  can be determined only for these events (Table 1). According to the MQS v.5 event catalog <  
354 20 % of these events have a SNR of < 2.0 in the 0.2 - 0.5 Hz frequency band. These are mostly quality  
355 'C' and 'D' events and their body-wave magnitudes are thus considered less certain.

356

357

### 358 **Calibration of 2.4Hz Magnitude $M_{2.4}^{Ma}$ Relative to $M_{W,spec}^{Ma}$**

359 Finally, we calibrate the 2.4Hz magnitude,  $M_{2.4}^{Ma}$ , which can be computed for all high-frequency  
360 events (*HF*, *VF*, *2.4Hz*) in the InSight v.5 catalog (Table 1). We assume a constant, magnitude-  
361 independent amplification of the 2.4 Hz resonance. We calibrate the resulting magnitudes to scale  
362 with  $M_{W,spec}^{Ma}$  for all high-frequency events that have additional measurements of  $A_0$  (*HF* and *8 VF*  
363 events: S0128a, S0264e, S0334a, S0376a, S0387a, S0421a, S0424c & S0475a, but no *2.4Hz*, see  
364 Table 1).

365

366 We define and calibrate the  $M_{2.4}^{\text{Ma}}$  in two ways:  $M_{2.4,\text{pick}}^{\text{Ma}}$  is calculated from the time domain  
 367 amplitude  $A_{2.4,\text{pick}}$ ;  $M_{2.4,\text{spec}}^{\text{Ma}}$  is calculated from the spectral amplitude  $A_{2.4,\text{spec}}$ . The first is  
 368 computed from the peak amplitude on the vertical component in the 2-3 Hz bandpass-filtered (6<sup>th</sup>  
 369 order Butterworth bandpass with corner frequencies of 2.2 Hz and 2.8 Hz) velocity waveform; the  
 370 second from fitting a Lorentz curve to the displacement spectra (computed as described in the  
 371 spectral magnitude section) between 2 and 3 Hz (Figure 2a).

372

373 From SNR-weighted amplitude regression of  $A_{2.4,\text{pick}}$  and  $A_{2.4,\text{spec}}$  with  $M_{W,\text{spec},\text{HF}}^{\text{Ma}}$ , we find

374

$$375 \quad M_{2.4,\text{pick}}^{\text{Ma}} = \log_{10}(A_{2.4,\text{pick}}) + 1.0 \log_{10}(\Delta) + 10.8 \quad (8a)$$

376 and

$$377 \quad M_{2.4,\text{spec}}^{\text{Ma}} = \log_{10}(A_{2.4,\text{spec}}) + 1.0 \log_{10}(\Delta) + 11.0 \quad (8b)$$

378

379

380

## 381 RESULTS

382 We use the event distances from the InSight MQS catalog v.5 (until 2020/10/12) and amplitudes  
 383 at different frequencies (as defined above) determined by MQS (Clinton *et al.*, 2020) to determine  
 384 magnitudes and uncertainties using the equations described above. Table S1 (Electronic  
 385 Supplement) summarizes all parameters and resulting magnitudes.

386

387 Overall, we achieve a very good agreement across the magnitude scales with standard deviations  
 388 of  $\sigma = 0.3$  for  $m_b^{\text{Ma}}$ ,  $m_{bS}^{\text{Ma}}$ , and of  $\sigma = 0.2$  for  $M_{2.4,\text{pick}}^{\text{Ma}}$  and  $M_{2.4,\text{spec}}^{\text{Ma}}$  with regards to the spectral  
 389 magnitude,  $M_{W,\text{spec}}^{\text{Ma}}$ , which we used as a calibration reference (Figure 4). There is basically no  
 390 difference between the sub-categories of the low- and high-frequency event families. The time  
 391 domain and spectral domain resonance magnitudes,  $M_{2.4,\text{pick}}^{\text{Ma}}$  and  $M_{2.4,\text{spec}}^{\text{Ma}}$ , are very similar, while  
 392  $M_{2.4,\text{spec}}^{\text{Ma}}$  achieves a slightly better fit with  $M_{W,\text{spec}}^{\text{Ma}}$ . We conclude that the two spectral magnitudes,  
 393  $M_{W,\text{spec}}^{\text{Ma}}$  and  $M_{2.4,\text{spec}}^{\text{Ma}}$ , are most robust and we thus set the preferred (moment) magnitude to

394  $M_W^{\text{Ma}} = M_{W,\text{spec},LF}^{\text{Ma}}$  for *LF* and *BB* events, to  $M_W^{\text{Ma}} = M_{W,\text{spec},HF}^{\text{Ma}}$  for *HF* events, and to  $M_W^{\text{Ma}} = M_{2.4,\text{spec}}^{\text{Ma}}$   
395 for *VF* and *2.4Hz* resonance events. The picking of peak amplitudes in the frequency domain is  
396 more stable, since a much longer time-window (5 - 30 minutes) is considered (Figure 2).

397

398 Adopting the newly calibrated scales (Table 2), we determine the magnitudes of the events in the  
399 InSight MQS catalog v.5 as  $1.1 \leq M_W^{\text{Ma}}(\sim M_W) \leq 3.7$  (Table S1). More specifically, we find  
400  $2.7 \leq M_W^{\text{Ma}} \leq 3.7$  for the 20 *LF* events,  $2.7 \leq M_W^{\text{Ma}} \leq 3.5$  for the 9 *BB* events,  $1.7 \leq M_W^{\text{Ma}} \leq 2.6$  for  
401 the 50 *HF* events,  $1.1 \leq M_W^{\text{Ma}} \leq 2.9$  for the 21 *VF* events, and  $1.3 \leq M_W^{\text{Ma}} \leq 3.0$  for the 179 *2.4Hz*  
402 events. From equation (5b) we estimate the magnitude uncertainties for the low-frequency (*LF*,  
403 *BB*) events to range between  $\sigma_M = 0.2$  and  $\sigma_M = 0.5$  (Table S1). As stated before, because of the  
404 currently unclear interpretation of high-frequency events, including their distances (Giardini *et al.*,  
405 2020; van Driel *et al.*, 2021), we simply set  $\sigma_M = 0.2$ , even though the true uncertainties could be  
406 much larger. Magnitude estimates for high-frequency events given in this article primarily serve  
407 for a relative comparison of these events with each other (see Discussion).

408

409 Figure 5 shows the distribution of all events as a function of epicentral distance. The four largest  
410 events are all low-frequency events: S0325a ( $M_W^{\text{Ma}} 3.7$ ,  $\Delta = 38^\circ$ , quality 'B'), S0167a ( $M_W^{\text{Ma}} 3.7$ ,  $\Delta =$   
411  $95^\circ$ , quality 'C'), S0173a ( $M_W^{\text{Ma}} 3.7$ ,  $\Delta = 28^\circ$ , quality 'A'), and S0235b ( $M_W^{\text{Ma}} 3.5$ ,  $\Delta = 27^\circ$ , quality 'A').  
412 Note that the distance estimate for S0167a is very uncertain, since it was derived from waveform  
413 envelope similarity (see Giardini *et al.*, 2020 for details). The large uncertainty in distance for  
414 S0167a is also reflected in inconsistent magnitude estimates across different scales ( $m_{\text{bS}}^{\text{Ma}} 3.3$  and  
415  $M_{W,\text{spec}}^{\text{Ma}} 3.7$ , see Table S1).

416

417

## 418 **DISCUSSION**

419 In this article, we recalibrated magnitude relations for Mars from InSight data using a seismicity  
420 catalog of a full Martian year, corresponding to nearly two Earth years. Pre-landing seismicity  
421 estimates expected larger marsquakes that more closely resembled teleseismic events we observe  
422 on Earth. Hence, our pre-landing magnitude study assumed larger events, with surface-waves and

423 energy at long periods (Böse *et al.*, 2018). An additional crucial difference from our pre-landing  
424 study is that the available data has included the routine collection of continuous high-sampled rate  
425 data (first 10 sps, then 20 sps) throughout the mission, instead of the 2 sps planned beforehand.  
426 This means higher frequency data than anticipated could be used. The high-frequency event class  
427 had not been expected at all and therefore required completely novel magnitude scales, as  
428 presented in this article.

429

430 (Single-station) magnitude computations are affected by assumptions made to model the seismic  
431 wave propagation from the source to the receiver. These models predict both the decay of seismic  
432 wave amplitudes and the observation of different phase arrivals at different distances, and they  
433 also impact the distance estimates relative to the receiver (Khan *et al.*, 2016). Despite collecting an  
434 exceptional seismic event dataset during the first year of the InSight mission (InSight Mars SEIS  
435 Data Service, 2019), our knowledge of Mars interior structure is still limited, which leads to  
436 unavoidable uncertainties in magnitude estimates.

437

438 Model assumptions have a strong impact on magnitude estimates as shown for the Moon.  
439 Nakamura *et al.* (1976) studied the distant-dependent decay of S-wave amplitudes on the Moon  
440 generated by artificial and meteoroid impacts as well as shallow moonquakes observed at the  
441 Apollo seismic network stations. The authors assigned lunar magnitudes to these events,  
442 estimated to be approximately 1.0 less than the Richter magnitude for the same amplitude. Goins  
443 *et al.* (1981) developed equations to estimate source parameters of shallow and deep moonquakes  
444 (seismic moment, seismic energy release, stress drop, and body-wave magnitude), from  
445 seismograms and displacement spectra that account for the effects of instrument bandwidth,  
446 variations in corner frequency, and the effects of intense scattering on the Moon. They determined  
447 the stress drops and body-wave magnitudes of the largest shallow moonquakes as 40 MPa, and ~  
448 5.0, respectively. Following the same method with some improvements and corrections, Oberst  
449 (1987) obtained remarkably different results with stress drops of > 100 MPa and body-wave  
450 magnitudes of > 5.5.

451



452 In our current understanding (Giardini *et al.*, 2020; van Driel *et al.*, 2021) the seismic waveforms  
 453 of events in the low-frequency (*LF*, *BB*) and high-frequency (*HF*, *VF*, 2.4Hz) event families are  
 454 dominated by mantle and crustal guided waves, respectively (Figures 1 and 2). Following this  
 455 interpretation, we constrained the magnitude scales in this article, assuming a volumetric seismic  
 456 wave propagation for the low-frequency and a surface propagation for the high-frequency events.

457

458 We determined the constant in equation (5a) from seismic waveform modeling through a set of  
 459 representative Mars models discussed in Clinton *et al.* (2017). From equations (2b) and (2c) and  
 460  $\Omega_0 \approx A_0 \sqrt{N \Delta t}$ , where  $N$  is the number of data samples before zero-padding in the time windows  
 461 and  $\Delta t$  the sampling interval of the displacement time series used for the PSD computation, we  
 462 would theoretically expect for S-waves that

463

$$464 \quad c_i = \log_{10}(\sqrt{N \Delta t}) + a_i \log_{10} \left( \frac{\pi}{180} R_{Ma} \right) + \log_{10} \frac{4\pi \rho v_s^3}{R_s^{\theta\phi} S_f} - 9.1 \quad (9)$$

465

466 With  $N = 512$ ,  $\Delta t = 0.05$  s,  $a_i = 1.0$ , density  $\rho = 3,500$  kg/m<sup>3</sup>,  $v_s = (3,500 \pm 500)$  m/s, average (S-  
 467 wave) radiation pattern of  $R_s^{\theta\phi} = 0.55$ , free-surface amplification  $S_f = 2.0$  (Boore & Boatwright,  
 468 1984), and radius of Mars  $R_{Ma} = 3'385$  km, we obtain  $c_i = 0.7 + 4.8 + (15.2 \pm 0.2) - 9.1 = (11.6$   
 469  $\pm 0.2)$ . The discrepancy between our modelled ( $c_i = 12.6$ ) and theoretical value ( $c_i = 11.6 \pm 0.2$ )  
 470 suggests that the theoretical approximation in equation (2b) is likely too simple for our purpose,  
 471 since we are not looking at a single seismic ray from the source through a full space, but at a time  
 472 window that contains both surface reflections and interfering rays. In fact, at the epicentral  
 473 distances of the observed marsquakes, the seismograms can no longer be regarded as the  
 474 deterministic signal that is assumed by the theory underlying equation (2b), but must be treated  
 475 as transient stochastic time series with variable amplitudes and undetermined duration.  
 476 Additional simulations based on the convolution of a synthetic source-time function of known  
 477 seismic moment with a transient white-noise time series multiplied with a tapering function that  
 478 decays exponentially with time show that the spectral analysis over a more or less arbitrary length  
 479 of the S-wave coda tends to underestimate the true seismic moment. Thus, at least part of the  
 480 difference between the theoretically expected value of  $c_i$  and the value of  $c_i$  derived from the

481 calibration procedure based on synthetic seismograms, implemented in the present study,  
 482 compensates for this methodological bias.

483

484 Despite the apparent disagreement with the theoretically expected  $c_i$  coefficient, the adequacy of  
 485 our magnitude scales is supported two-fold: (1) In an independent study, Brinkman *et al.* (2020)  
 486 determined the magnitudes of the S0235b, S0173a, and S0183a events from moment tensor  
 487 inversion as  $M_W$ 3.1,  $M_W$ 3.0, and  $M_W$ 3.3, respectively, which is close to our values ( $M_W^{\text{Ma}}$ 3.5  $\pm$  0.3,  
 488  $M_W^{\text{Ma}}$ 3.7  $\pm$  0.4, and  $M_W^{\text{Ma}}$ 3.1  $\pm$  0.4 respectively; see Table S1). The remaining discrepancy can be  
 489 explained, since for S0235b and S0173a, the InSight station is located close to a maximum of the  
 490 S-wave radiation pattern (as estimated from the amplitude  
 491 ratios of P- and S-waves on different components), resulting in an overestimation of magnitude  
 492 when not inverting for the moment tensor. (2) Figure 6 compares our  $m_b^{\text{Ma}}$  and  $m_{bS}^{\text{Ma}}$  estimates  
 493 from  $A_P$  and  $A_S$  for the low-frequency (*LF*, *BB*) events in the InSight catalog with the medium-  
 494 period body-wave broadband magnitude,  $mB$ , proposed by Gutenberg (1945a,b) for Earth.  
 495 Although developed for teleseismic P- and S-waves at 2 - 20 s period on Earth (Bormann *et al.*,  
 496 2013), we are applying the  $mB$  relations here to Mars for  $A_P$  and  $A_S$  at 2 - 6 s period. Simplifying  
 497 the lookup table in Gutenberg and Richter (1956) for a source depth of 15 km and two distance  
 498 intervals, we obtain

499

$$500 \quad mB_P = \log_{10}(A_P) + 12.9 \text{ for } \Delta \leq 70^\circ \quad (10a)$$

$$501 \quad mB_P = \log_{10}(A_P) + 13.2 \text{ for } \Delta > 70^\circ \quad (10b)$$

$$502 \quad mB_S = \log_{10}(A_S) + 12.6 \text{ for } \Delta \leq 70^\circ \quad (10c)$$

$$503 \quad mB_S = \log_{10}(A_S) + 13.0 \text{ for } \Delta > 70^\circ \quad (10d)$$

504

505 The good agreement of  $m_b^{\text{Ma}}$  and  $m_{bS}^{\text{Ma}}$  with  $mB_P$  and  $mB_S$  in Figure 6 suggests that the attenuation  
 506 of body-waves at long periods and teleseismic distances on Mars and Earth are similar. While we  
 507 could potentially consider applying earthquake magnitude scales, such as  $mB$ , to Mars, it needs to  
 508 be pointed out again that due to the noise condition on Mars, time-domain amplitudes  $A_P$  and  $A_S$   
 509 could so far be determined only for a small subset of marsquakes. For the majority of seismic  
 510 events we have only measurements of spectral amplitudes ( $A_0$ ,  $A_{2.4,\text{spec}}$ ) for which no comparable

511 magnitude scales on Earth exist. On the other hand, the good agreement of mars- and earthquake  
512 magnitude scales in Figure 6 indicates that both the absolute calibration of  $M_{W,spec}^{Ma}$  and the  
513 relative calibration of (at least) of  $m_b^{Ma}$  and  $m_{bS}^{Ma}$  achieve reasonable magnitude estimates.

514

515 All marsquake signals identified by MQS so far have durations of 5 to 30 minutes. This is  
516 significantly longer compared to what we would expect on Earth for the same magnitude range ( $M$   
517  $< 4$ ), even though the comparison is difficult since such small events are usually not observed  
518 in distances of  $> 1500$  km. We attribute these long durations mainly to the strong scattering of  
519 seismic energy on Mars (e.g., Lognonné *et al.*, 2020). On Earth, the signal length has been used to  
520 compute duration (or coda) magnitudes for strong historical and local earthquakes (Bormann *et al.*  
521 *et al.*, 2013). On Mars, such a relationship, however, is not clearly visible, likely because scattering is  
522 the dominating effect on the signal duration, which is independent of the source magnitude.

523

524 Distances of low-frequency (*LF*, *BB*) events relative to the InSight lander in the event catalog  
525 (InSight Marsquake Service, 2021) were determined using the probabilistic approach of Böse *et al.*  
526 (2016), which accounts for both pick and model uncertainties. This approach requires at least 2  
527 seismic phase picks. Absolute event locations in the catalog (including a backazimuth) were  
528 inferred only for events with a clear polarization of the seismic signals, which only applies to a  
529 small subset of events (Clinton *et al.*, 2020). As discussed in Böse *et al.* (2018), even large distance  
530 uncertainties on the order of 25% and depth errors of 20 km (L1 InSight mission requirements;  
531 Banerdt *et al.*, 2013) translate into magnitude errors of only  $\pm 0.2$  units, which is smaller than the  
532 magnitude uncertainties ( $\pm 0.5$  units) that can generally be expected with a single-station approach  
533 and that are related to the variability in the focal mechanisms and uncertainties in the interior  
534 model.

535

536 A number of low-frequency events without clear emergent phase arrivals in the InSight catalog  
537 were located based on the similarity of waveform envelopes and theoretical travel-time curves  
538 using locatable events with clear phases as a reference (Giardini *et al.*, 2020). Estimating the  
539 distance (and thus magnitude) uncertainties for these events is difficult. They might be quite large,  
540 in particular for events at large distances. Phase identification for these events is ambiguous, some

541 of them have extremely weak P- and S-wave signals (Giardini *et al.*, 2020). For instance, it is  
542 possible that  $A_p$  (and potentially  $A_s$ ) for the most distant marsquake (S0167a) at 95° distance was  
543 measured in a different phase than for the closer events, or that the event is even beyond the core  
544 shadow and we observe a SS/SSS wave train. This would also explain the different shape of the  
545 waveform envelopes as observed in Giardini *et al.* (2020). For this reason, we consider the current  
546 magnitude estimates for S0167a and other events in this distance range to be rather uncertain.  
547 Further research is needed to better understand the seismic wave propagation through Mars,  
548 which will lead to a better phase assignment and enhanced distance and thus magnitude estimates  
549 in the future.

550

551 Locating the (crustal) high-frequency (*HF*, *VF*, *2.4Hz*) events requires another approach. In the  
552 InSight catalog distances of these events were inferred from  $P_g$ - $S_g$  travel-times using a very simple  
553 model with constant velocities of  $v_p = 4$  km/s and  $v_s = v_p/\sqrt{3}$  (= 2.3 km/s) (van Driel *et al.*,  
554 2021). With this model, high-frequency events are located at distances between 3° and 40°, with  
555 the bulk between 25 and 30°, while low-frequency events are located at 20° - 95° distance (Figure  
556 5). Assuming lower (e.g.  $v_p = 2.6$  km/s and  $v_s = 1.5$  km/s) or higher (e.g.  $v_p = 5.2$  km/s and  $v_s =$   
557  $3.0$  km/s) velocities, the distances of the high-frequency events would change by approximately  
558 10° (1° on Mars corresponds to 59.2 km). Using equation (6b), this translates again into magnitude  
559 uncertainties of  $\pm 0.2$  units, similarly to the expected uncertainties for low-frequency events, and  
560 again smaller compared to what can generally be expected with a single station approach ( $\pm 0.5$   
561 units). Because of the currently unclear interpretation of events in the high-frequency family,  
562 including large uncertainties in their distances, our magnitude estimates for these events serve  
563 primarily to enable a relative comparison of these events with each other.

564

565 Models of the subsurface structure of Mars below the InSight lander start emerging. For example,  
566 the receiver function analysis of Lognonné *et al.* (2020) suggests a 10 km low-velocity layer, which  
567 might generate some type of site effect. The 2.4 Hz resonance is probably caused by even shallower  
568 layers, but these are most likely not the ones in which the guided waves of the high-frequency  
569 events propagate (van Driel *et al.*, 2021). Nevertheless, the propagation velocity of the guided

570 waves could significantly differ from those we assumed at the source, resulting in a systematic bias  
571 in the moment estimation. Incorporating site effects as predicted from this and other models,  
572 which are currently being developed, could help to fine-tune magnitude estimates on Mars in the  
573 future.

574

575

## 576 **CONCLUSIONS & OUTLOOK**

577 In this article, we revised the magnitude relations in Böse *et al.* (2018) to account for the seismic  
578 and noise characteristics observed on Mars during the first Martian year of the InSight mission. In  
579 light of these observations, we updated the scaling relations for the spectral and body-wave  
580 magnitudes,  $M_{W,spec}^{Ma}$ ,  $m_b^{Ma}$  and  $m_{bS}^{Ma}$ , and introduced a new magnitude scale,  $M_{2.4}^{Ma}$ , for high-  
581 frequency events. The new scales are summarized in Table 2 of this article. We recommend setting  
582 the preferred magnitude to  $M_W^{Ma} = M_{W,spec,LF}^{Ma}$  for *LF* and *BB* events, to  $M_W^{Ma} = M_{W,spec,HF}^{Ma}$  for *HF*  
583 events, and to  $M_W^{Ma} = M_{2.4,spec}^{Ma}$  for *VF* and *2.4Hz* resonance events. We used the new magnitude  
584 scales to determine that the magnitudes of the events in the current InSight catalog v.5 range  
585 between 1.1 and 3.7. We estimate that magnitude uncertainties are on the order of  $\pm 0.5$  magnitude  
586 units, which is mainly due to uncertainties in the focal mechanisms rather than in distances.  
587 Location uncertainties of some events in the InSight catalog, however, might be quite large, in  
588 particular for events at large distance with uncertain phase identification. Estimating the  
589 magnitude uncertainties of these events is difficult, in particular because other phase arrivals  
590 might be measured than what was used for magnitude calibration. Overall, we achieve a very good  
591 agreement across all magnitude scales with regards to the spectral magnitude,  $M_{W,spec}^{Ma}$ , which is  
592 considered a measure of the moment magnitude,  $M_W$ .

593

594 Magnitude estimates of marsquakes are a key component in the characterization of the seismic  
595 activity rate of Mars (Knapmeyer *et al.*, 2019). All pre-mission Martian seismicity models are based  
596 on estimated moment rates, which require magnitudes. Hence, magnitudes are needed to  
597 determine which models are best suited for Mars. Refining interior models of Mars from InSight  
598 observations will not only help to further refine magnitude scales for marsquakes in the future,

599 but also to better understand the level and distribution of seismicity on the planet. Once we have  
600 a better understanding of the source and propagation, in particular of *VF* and *SF* events, new  
601 magnitudes scales for these events will be devised.

602

603

## 604 **DATA & RESOURCES**

605 The Electronic Supplement to this article contains source parameters of marsquakes as provided  
606 in the InSight catalog v.5 (until 2020/10/12) of the InSight Marsquake Service (2021), as well as  
607 time-domain and spectral amplitudes, spectral fitting parameters and magnitudes as computed in  
608 this article.

609 InSight Marsquake Service (2021). Mars Seismic Catalogue, InSight Mission; V5 2021-01-04. ETHZ,  
610 IPGP, JPL, ICL, MPS, Univ. Bristol. <https://doi.org/10.12686/a10>.

611 InSight Mars SEIS Data Service (2019). SEIS raw data, InSight Mission. IPGP, JPL, CNES, ETHZ, ICL,  
612 MPS, ISAE-Supaero, LPG, MFSC. <https://doi.org/10.18715/SEIS.INSIGHT.XB.2016>.

613 InSight Mars SEIS Data Service (2019). InSight SEIS Data Bundle. PDS Geosciences (GEO) Node.  
614 <https://doi.org/10.17189/1517570>.

615 Please be aware that the InSight catalog can change over time reflecting our respective  
616 understanding of Mars seismicity and its interior structure. The most recent event InSight catalog  
617 can be retrieved from <https://www.iris.edu/hq/sis/insight>.

618

619

## 620 **ACKNOWLEDGEMENTS**

621 We would like to thank two anonymous reviewers, Guest Editor Sharon Kedar and Editor-in-Chief  
622 Thomas Pratt for their positive feedback and comments. We acknowledge NASA, CNES, their  
623 partner agencies and institutions (UKSA, SSO, DLR, JPL, IPGP-CNRS, ETHZ, IC, MPS-MPG) and the  
624 flight operations team at JPL, SISMOC, MSDS, IRIS-DMC and PDS for providing SEED SEIS data. We  
625 acknowledge funding from (1) Swiss State Secretariat for Education, Research and Innovation  
626 (SEFRI project “MarsQuake Service-Preparatory Phase”), (2) ETH Research grant ETH-06 17-02,  
627 and (3) ETH+02 19-1: Planet MARS. The Swiss contribution in implementation of the SEIS

628 electronics was made possible through funding from the federal Swiss Space Office (SSO), the  
629 contractual and technical support of the ESA-PRODEX office. The French authors acknowledge the  
630 French Space Agency CNES and ANR (ANR-14-CE36-0012-02 and ANR-19-CE31-0008-08) for  
631 support in the Science analysis. This is InSight contribution #186.

632 **REFERENCES**

- 633 Aki, K., & Richards, P. G. (1980). *Quantitative seismology: Theory and methods*. San Francisco: W.H.  
634 Freeman.
- 635 Banerdt, W. B., S. Smrekar, P. Lognonné, T. Spohn, S. W. Asmar, D. Banfield, L. Boschi, U. Christensen,  
636 V. Dehant, W. Folkner, et al. (2013). InSight: A discovery mission to explore the interior of Mars,  
637 Lunar and Planetary Science Conference, Lunar and Planetary Institution. Technical Report,  
638 Vol. 44, 1915 pp.
- 639 Banerdt, W.B., S. Smrekar, P. Lognonné, D. Giardini, et al. (2020). Early Results from the InSight  
640 Mission: Surface Environment and Global Seismic Activity, *Nature Geoscience*, 13, 183–  
641 189(2020), doi: 10.1038/s41561-020-0544-y.
- 642 Basham, P. W. (1971). A New Magnitude Formula for Short Period Continental Rayleigh  
643 Waves, *Geophys. J. Int.* 23(2), 255–260, <https://doi.org/10.1111/j.1365-246X.1971.tb01817.x>.
- 644 Bisztricsany, E. (1958). *A new method for the determination of the magnitude of earthquake*. *Geofiz.*  
645 *Kozl.*, 7, 69-96 (in Hungarian with English abstract).
- 646 Brune, J. N. (1970). Tectonic stress and the spectra of seismic shear waves from earthquakes, *J.*  
647 *Geophys. Res.*, 75(26), 4997–5009, doi:10.1029/JB075i026p04997.
- 648 Böse, M., Clinton, J. F., Ceylan, S., Euchner, F., van Driel, M., Khan, A., et al. (2016). A Probabilistic  
649 Framework for Single-Station Location of Seismicity on Earth and Mars. *Physics of the Earth and*  
650 *Planetary Interiors*, 262, 48–65. <https://doi.org/10.1016/j.pepi.2016.11.003>
- 651 Böse, M., Giardini, D., Stähler, S. C., Ceylan, S., Clinton, J. F., van Driel, M., et al. (2018). Magnitude  
652 Scales for Marsquakes. *Bull. Seismol. Soc. Am.* 108(5A), 2764–2777.  
653 <https://doi.org/10.1785/0120180037>
- 654 Boore, D., and J. Boatwright (1984). Average body-wave radiation coefficients, *Bull. Seism. Soc. Am.*,  
655 74, 1615-1621.
- 656 Bormann, P., S. Wendt, D. DiGiacomo (2013). Seismic sources and source parameters, In: Bormann,  
657 P. (Ed.), *New Manual of Seismological Observatory Practice 2 (NMSOP2)*, Potsdam, Deutsches  
658 GeoForschungsZentrum GFZ, 1-259, [https://doi.org/10.2312/GFZ.NMSOP-2\\_ch3](https://doi.org/10.2312/GFZ.NMSOP-2_ch3).
- 659 Brinkman, N., S. Stähler, D. Giardini, C. Schmelzbach, A. Jacob, N. Fuji, C. Perrin, P. Lognonné, M.  
660 Böse, B. Knapmeyer-Endrun, E. Beucler, E. et al. (2020). Single-station moment tensor inversion  
661 on Mars, *J. Geophys. Res. – Planets*, 10.1002/essoar.10503341.1.
- 662 Ceylan, S., van Driel, M., Euchner, F., Khan, A., Clinton, J., Krischer, L., Böse, M., Stähler, S. and D.  
663 Giardini (2017). From initial models of seismicity, structure and noise to synthetic  
664 seismograms for Mars, *Space Science Reviews*, InSight special issue, DOI 10.1007/s11214-017-  
665 0380-6.
- 666 Ceylan, S., J. Clinton, D. Giardini, M. Böse, C. Charalambous, et al. (2020). Companion guide to the  
667 Marsquake catalog from InSight, sols 0–478: Data content and non-seismic events, *Physics of*  
668 *the Earth and Planetary Interiors*, <https://doi.org/10.1016/j.pepi.2020.106597>
- 669 Charalambous, C., Stott, A. E., Pike, W. T., McClean, J. B., Warren, T., Spiga, A., et al. (2021). A  
670 Comodulation Analysis of Atmospheric Energy Injection into the Ground Motion at InSight,  
671 Mars. *Journal of Geophysical Research: Planets* 126,  
672 e2020JE006538. <https://doi.org/10.1029/2020JE006538>
- 673 Clinton, J. F., Giardini, D., Böse, M., Ceylan, S., van Driel, M., Euchner, F., et al. (2018). The Marsquake  
674 Service: Securing Daily Analysis of SEIS Data and Building the Martian Seismicity Catalogue for  
675 InSight. *Space Science Reviews*, 214(8), 133. doi:10.1007/s11214-018-0567-5.
- 676 Clinton, J. F., D. Giardini, P. Lognonné, B. Banerdt, M. van Driel, M. Drilleau, N. Murdoch, M. Panning,  
677 R. Garcia, D. Mimoun, M. Golombek, J. Tromp, R. Weber, M. Böse, S. Ceylan, I. Daubar, B. Kenda,  
678 A. Khan, L. Perrin, and A. Spiga (2017). Preparing for InSight: an invitation to participate in a  
679 blind test for Martian seismicity, *Seismol. Res. Lett.* 88(5), 1290-1302, doi:  
680 10.1785/0220170094.
- 681 Clinton, J.F., S. Ceylan, M. van Driel, D. Giardini, S.C. Stähler, M. Böse et al. (2020). The Marsquake  
682 Catalogue from InSight, Sols 0-478, *Physics of the Earth and Planetary Interiors*,  
683 <https://doi.org/10.1016/j.pepi.2020.106595>.
- 684 Dahmen, N. L., Clinton, J. F., Ceylan, S., van Driel, M., Giardini, D., Khan, A., et al. (2021). Super  
685 high frequency events: A new class of events recorded by the InSight seismometers on



686 Mars. *Journal of Geophysical Research: Planets* 126,  
687 e2020JE006599. <https://doi.org/10.1029/2020JE006599>  
688 Dahmen, N., G. Zenhäusern, et al. (subm.): Resonances and Lander Modes observed  
689 by InSight on Mars (1-9~Hz), submitted to BSSA.  
690 Giardini, D., P. Lognonné, W. Banerdt, W. Pike, U. Christensen, S. Ceylan, J. Clinton, M. van Driel, S.  
691 Stähler, M. Böse *et al.* (2020). The Seismicity of Mars, *Nature Geoscience*, 13, 1-8, doi:  
692 10.1038/s41561-020-0539-8.  
693 Goins, N.R., A.M. Dainty, and M.N. Toksöz (1981). Seismic energy release of the Moon, *J. Geophys.*  
694 *Res.* 86: 378–388.  
695 Gutenberg, B. (1945a). Amplitudes of P, PP, and S and magnitude of shallow earthquakes. *Bull.*  
696 *Seism. Soc. Am.* 35, 57-69.  
697 Gutenberg, B. (1945b). Magnitude determination of deep-focus earthquakes. *Bull. Seism. Soc. Am.*,  
698 35, 117-130.  
699 Gutenberg, B., and Richter, C. F. (1956). Magnitude and energy of earthquakes, *Annali di Geofisica*,  
700 9, 1-15.  
701 Hanks, T.C. and H. Kanamori (1979). A Moment magnitude scale, *J. Geophys. Res.* 84 (B5),  
702 doi:10.1029/JB084iB05p02348.  
703 InSight Mars SEIS Data Service (2019). SEIS raw data, InSight Mission. IPGP, JPL, CNES, ETHZ, ICL,  
704 MPS, ISAE-Supaero, LPG, MFSC. <https://doi.org/10.18715/SEIS.INSIGHT.XB.2016>.  
705 InSight Mars SEIS Data Service (2019). InSight SEIS Data Bundle. PDS Geosciences (GEO) Node.  
706 <https://doi.org/10.17189/1517570>.  
707 InSight Marsquake Service (2021). Mars Seismic Catalogue, InSight Mission; V5 2021-01-04. ETHZ,  
708 IPGP, JPL, ICL, MPS, Univ. Bristol. <https://doi.org/10.12686/a10>.  
709 Kennett, B. L. N. and T. Furumura (2013). High-frequency *Po/So* guided waves in the oceanic  
710 lithosphere: I—long-distance propagation, *Geophysical Journal International* 195(3), 1862–  
711 1877, <https://doi.org/10.1093/gji/ggt344>.  
712 Khan, A., van Driel, M., Böse, M., Giardini, D., Ceylan, S., Yan, J., . . . Banerdt, W. B. (2016). Single-  
713 station and single-event marsquake location and inversion for structure using synthetic  
714 Martian waveforms, *Phys. Earth Planet. Inter.* 258, 28-42. doi:  
715 <https://doi.org/10.1016/j.pepi.2016.05.017>.  
716 Knapmeyer, M., B. Knapmeyer-Endrun, A.-C. Plesa, M. Böse, T. Kawamura, J.F. Clinton, M.P.  
717 Golombek, S. Kedar, S. Stähler, J. Stevanović, C. Perrin, P. Lognonné, N.A. Teanby, and R. Weber  
718 (2019). Estimation of the Seismic Moment Rate from an Incomplete Seismicity Catalog, in the  
719 Context of the InSight Mission to Mars, *Bull. Seismol. Soc. Am.*, 109 (3), 1125-1147,  
720 <https://doi.org/10.1785/0120180258>.  
721 Lognonné, P., W. B. Banerdt, D. Giardini, W. T. Pike, U. Christensen, and et al. (2020). First  
722 constraints on the shallow elastic and anelastic structure of Mars from InSight data, *Nature*  
723 *Geoscience*, 13, 213-220, doi: 10.1038/s41561-020-0536-y.  
724 Lognonné, P., Banerdt, W. B., Giardini, D., Pike, W. T., Christensen, U., Laudet, P., et al. (2019). SEIS:  
725 InSight’s Seismic Experiment for Internal Structure of Mars. *Space Science Reviews*, 215(1), 12.  
726 <https://doi.org/10.1007/s11214-018-0574-6>  
727 Mimoun, D., Murdoch, N., Lognonné, P., Hurst, K., Pike, W.T., Hurley, J., Nebut, T. & Banerdt, W.B.  
728 (2017). The Noise Model of the SEIS Seismometer of the InSight Mission to Mars, *Space Science*  
729 *Review*, doi: 10.1007/s11214-017-0409-x.  
730 Nakamura, Y., Duennebier, F. K., Latham, G. V., and Dorman, H. J. (1976). Structure of the lunar  
731 mantle, *J. Geophys. Res.*, 81( 26), 4818– 4824, doi:[10.1029/JB081i026p04818](https://doi.org/10.1029/JB081i026p04818).  
732 Nissen-Meyer, T., van Driel, M., Stähler, S. C., Hosseini, K., Hempel, S., Auer, L., Colombi, A., &  
733 Fournier, A. (2014). AxiSEM: broadband 3-D seismic wavefields in axisymmetric media. *Solid*  
734 *Earth*, 5(1), 425–445. <https://doi.org/10.5194/se-5-425-2014>.  
735 Nuttli, O. W. (1973). Seismic wave attenuation and magnitude relations for eastern North  
736 America, *J. Geophys. Res.*, 78( 5), 876– 885, doi:[10.1029/JB078i005p00876](https://doi.org/10.1029/JB078i005p00876).  
737 Oberst, J. (1987). Unusually high stress drop associated with shallow moonquakes, *J. Geophys. Res.*  
738 92: 1397–1405.  
739 van Driel, M., Ceylan, S., Clinton, J. F., Giardini, D., Horleston, A., Margerin, L., et al. (2021). High-  
740 frequency seismic events on Mars observed by InSight. *Journal of Geophysical Research:*  
741 *Planets*, 126, e2020JE006670. <https://doi.org/10.1029/2020JE006670>

742 van Driel, M., Krischer, L., Stähler, S. C., Hosseini, K., and T. Nissen-Meyer (2015). Instaseis: instant  
743 global seismograms based on a broadband waveform database, *Solid Earth* 6, 701-717,  
744 <http://dx.doi.org/10.5194/se-6-701-2015>.

745 **Mailing Address for each Author**

746 **Maren Böse**, Institute of Geophysics, Swiss Seismological Service (SED), ETH Zurich, Sonneggstr.  
747 5, 8092 Zurich, Switzerland; [mboese@sed.ethz.ch](mailto:mboese@sed.ethz.ch), <https://orcid.org/0000-0003-4639-719X>

748  
749 **Simon Stähler**, Institute of Geophysics, ETH Zürich, Sonneggstrasse 5, 8092 Zürich, Switzerland;  
750 [simon.staehler@erdw.ethz.ch](mailto:simon.staehler@erdw.ethz.ch), <https://orcid.org/0000-0002-0783-2489>

751  
752 **Nicholas Deichmann**, Swiss Seismological Service (SED), ETH Zurich, Sonneggstr. 5, 8092 Zurich,  
753 Switzerland; [deichmann@sed.ethz.ch](mailto:deichmann@sed.ethz.ch)

754  
755 **Domenico Giardini**, Institute of Geophysics, ETH Zurich, Sonneggstr. 5, 8092 Zurich, Switzerland;  
756 [domenico.giardini@erdw.ethz.ch](mailto:domenico.giardini@erdw.ethz.ch), <https://orcid.org/0000-0002-5573-7638>

757  
758 **John Clinton**, Swiss Seismological Service (SED), ETH Zurich, Sonneggstr. 5, 8092 Zurich,  
759 Switzerland; [jclinton@sed.ethz.ch](mailto:jclinton@sed.ethz.ch), <https://orcid.org/0000-0001-8626-2703>

760  
761 **Philippe Lognonné**, Université de Paris, Institut de physique du globe de Paris, CNRS, F-75005  
762 Paris, France; [lognonne@ipgp.fr](mailto:lognonne@ipgp.fr), <https://orcid.org/0000-0002-1014-920X>

763  
764 **Savas Ceylan**, Institute of Geophysics, ETH Zurich, Sonneggstr. 5, 8092 Zurich, Switzerland;  
765 [savas.ceylan@erdw.ethz.ch](mailto:savas.ceylan@erdw.ethz.ch); <https://orcid.org/0000-0002-6552-6850>

766  
767 **Martin van Driel**, Institute of Geophysics, ETH Zurich, Sonneggstr. 5, 8092 Zurich, Switzerland;  
768 [vandriel@erdw.ethz.ch](mailto:vandriel@erdw.ethz.ch), <https://orcid.org/0000-0002-8938-4615>

769  
770 **Constantinos Charalambous**, Department of Electrical and Electronic Engineering, Imperial  
771 College London, South Kensington Campus, London, SW7 2AZ, United Kingdom;  
772 [constantinos.charalambous@imperial.ac.uk](mailto:constantinos.charalambous@imperial.ac.uk), <https://orcid.org/0000-0002-9139-3895>

773  
774 **Nikolaj Dahmen**, Institute of Geophysics, ETH Zurich, Sonneggstr. 5, 8092 Zurich, Switzerland;  
775 [nikolaj.dahmen@erdw.ethz.ch](mailto:nikolaj.dahmen@erdw.ethz.ch), <https://orcid.org/0000-0002-9114-6747>

776  
777 **Anna Horleston**, School of Earth Sciences, University of Bristol, Wills Memorial Building, Queens  
778 Road, Bristol BS8 1RJ, UK; [anna.horleston@bristol.ac.uk](mailto:anna.horleston@bristol.ac.uk), <https://orcid.org/0000-0002-6748-6522>

779  
780  
781 **Taichi Kawamura**, Université de Paris, Institut de physique du globe de Paris, CNRS, F-75005  
782 Paris, France; [kawamura@ipgp.fr](mailto:kawamura@ipgp.fr)

783  
784 **Amir Khan**, Institute of Geophysics, ETH Zurich, Sonneggstr. 5, 8092 Zurich,  
785 Switzerland; [akhan@ethz.ch](mailto:akhan@ethz.ch), <https://orcid.org/0000-0003-4462-3173>

786  
787 **Martin Knapmeyer**, DLR Institute of Planetary Research, Rutherfordstr. 2, 12489 Berlin,  
788 Germany; [martin.knapmeyer@dlr.de](mailto:martin.knapmeyer@dlr.de), <https://orcid.org/0000-0003-0319-2514>

789  
790 **Guénolé Orhand-Mainsant**, Institut Supérieur de l'Aéronautique et de l'Espace SUPAERO, 10  
791 Avenue Edouard Belin, 31400 Toulouse, France; [guenole.orhand-mainsant@isae-supaero.fr](mailto:guenole.orhand-mainsant@isae-supaero.fr),  
792 <https://orcid.org/0000-0003-4923-5241>

793

794 **John-Robert Scholz**, Max Planck Institute for Solar System Research, Justus-von-Liebig-Weg 3,  
795 37077 Göttingen, Germany; [scholz@mps.mpg.de](mailto:scholz@mps.mpg.de), <https://orcid.org/0000-0003-1404-2335>  
796  
797 **Fabian Euchner**, Institute of Geophysics, ETH Zurich, Sonneggstr. 5, 8092 Zurich, Switzerland;  
798 [fabian.euchner@sed.ethz.ch](mailto:fabian.euchner@sed.ethz.ch), <https://orcid.org/0000-0001-6340-7439>  
799  
800 **W. Bruce Banerdt**, Jet Propulsion Laboratory, California Institute of Technology, Pasadena, CA  
801 91109, USA; [bruce.banerdt@jpl.nasa.gov](mailto:bruce.banerdt@jpl.nasa.gov), <https://orcid.org/0000-0003-3125-1542>

802 **Tables**

803

804 **Table 1.** Number of seismic events for different event families and categories in the InSight v.5  
 805 catalog (until 2020/10/12; InSight Marsquake Service, 2021) that we use for magnitude  
 806 calibration of four magnitude scales: spectral magnitude,  $M_{w,spec}^{Ma}$ , P- and S-body-wave  
 807 magnitudes,  $m_b^{Ma}$  and  $m_{bS}^{Ma}$ , and 2.4 Hz magnitude,  $M_{2.4}^{Ma}$ . We only use events with distance  
 808 estimates. Four events (S0183a, S205a, S0325a and S0357a, see Table S1) are excluded from the  
 809 calibration of  $m_{bS}^{Ma}$ , because they fall into the low (S-wave) amplitude-zone of Mars (Giardini *et*  
 810 *al.*, 2020).  $M_{w,spec}^{Ma}$  is used as a calibration reference for the other scales for events with multiple  
 811 amplitude measurements: it is most closely related to the moment magnitude  $M_w$ , less affected  
 812 by noise, and can be determined for three out of five event categories.

Event family	Event category	Number of events	$M_{w,spec}^{Ma}$ spectral domain	$m_b^{Ma}$ time domain	$m_{bS}^{Ma}$ time domain	$M_{2.4}^{Ma}$ spectral or time domain
Low-frequency	Low-frequency (LF)	20	20	20	16	-
	Broadband (BB)	9	9	9	8	-
High-frequency	High-frequency (HF)	50	50	-	-	50
	Very high-frequency (VF)	21	8	-	-	21
	2.4 Hz resonance (2.4Hz)	179	-	-	-	179

813

814 **Table 2.** Resulting magnitude scales for marsquakes. Spectral amplitudes  $A_0$  (at 20 – 100 s) and  
815  $A_{2.4,spec}$  (at 2 – 3 Hz) are in  $m/\sqrt{Hz}$ , time domain amplitudes  $A_P$ ,  $A_S$  (both at 0.2 - 0.5 Hz) and  
816  $A_{2.4,pick}$  (at 2 – 3 Hz) in  $m$ , and epicentral distance  $\Delta$  in  $^\circ$  [degrees].

Name	Equation	Event family & categories	Calibrated Distance Range
Spectral magnitude	$M_{W,spec,LF}^{Ma} = 2/3(\log_{10}(A_0) + (1.0 \pm 0.1) \log_{10}(\Delta) + (12.6 \pm 0.5))$	Low-frequency (LF, BB)	$25^\circ \leq \Delta \leq 100^\circ$
Spectral magnitude	$M_{W,spec,HF}^{Ma} = 2/3(\log_{10}(A_0) + (0.8 \pm 0.1) \log_{10}(\Delta) + 12.8)$	High-frequency (HF, VF)	$3^\circ \leq \Delta \leq 30^\circ$
Body-wave magnitude (P-wave)	$m_b^{Ma} = \log_{10}(A_P) + 0.73 \log_{10}(\Delta) + 11.8$	Low-frequency (LF, BB)	$25^\circ \leq \Delta \leq 100^\circ$
Body-wave magnitude (S-wave)	$m_{bS}^{Ma} = \log_{10}(A_S) + 1.06 \log_{10}(\Delta) + 10.9$	Low-frequency (LF, BB)	$25^\circ \leq \Delta \leq 35^\circ$ $60^\circ \leq \Delta \leq 100^\circ$
2.4Hz magnitude (time domain)	$M_{2.4,pick}^{Ma} = \log_{10}(A_{2.4,pick}) + 1.0 \log_{10}(\Delta) + 10.8$	High-frequency (VF, HF, 2.4Hz)	$3^\circ \leq \Delta \leq 35^\circ$
2.4Hz magnitude (spectral domain)	$M_{2.4,spec}^{Ma} = \log_{10}(A_{2.4,spec}) + 1.0 \log_{10}(\Delta) + 11.0$	High-frequency (VF, HF, 2.4Hz)	$3^\circ \leq \Delta \leq 35^\circ$

817

818 **Figure Captions**

819

820 **Figure 1. Seismic wave propagation on Mars.** The current interpretation of seismic signals on  
821 Mars is that events in the high-frequency event family (*HF, VF*) excite guided waves in the crust or  
822 in a shallow layer, while events in the low-frequency family (*LF, BB*) are located below the Moho;  
823 these mantle waves are observed at long periods due to attenuation. A low-velocity layer (LVL)  
824 could potentially explain the observed distant-dependent variation of S-wave amplitudes.  
825 Modified after Giardini *et al.* (2020).

826

827 **Figure 2. Amplitude computation from marsquake spectra and waveforms.** (a) Theoretical  
828 spectral shape of power spectral density (PSD) displacement spectra for events of the low-  
829 frequency (*LF, BB*; red) and high-frequency (*HF, VF*; blue) event families for various magnitudes.  
830 Black line shows typical background noise. (b) Filtered displacement waveforms (vertical  
831 component). Spectral amplitudes  $A_0$  and  $A_{2.4,spec}$  in (a) are determined from the long-period  
832 plateau of the event displacement spectra and from a Lorentz curve fitted to the 2.4 Hz resonance  
833 peak, respectively. Peak displacement amplitudes  $A_P$  and  $A_S$  in (b) are determined from the  
834 filtered (2 - 6 s, top) displacement waveforms in the time window of the P- or S-wave arrivals. Note  
835 that  $A_S$  is actually picked on the horizontals, while we only show vertical components for the sake  
836 of simplicity.  $A_{2.4,pick}$  in (b) is determined from the peak amplitude of the 2-3 Hz filtered  
837 displacement waveform (bottom). Subplots in (c) and (d) show example spectra and waveforms  
838 (vertical components) of representative marsquakes of each event category: *LF* – low-frequency,  
839 *BB* – broadband, *HF* – high-frequency, *VF* – very high-frequency, and *2.4Hz* – 2.4Hz ambient  
840 resonance event.

841

842 **Figure 3. Magnitude calibration for marsquakes.** First, we calibrate the spectral magnitude  
843  $M_{W,spec}^{Ma}$  from synthetic waveforms and theoretical considerations (see main text). Then we  
844 calibrate the other magnitude scales (body-wave magnitudes  $m_b^{Ma}$  and  $m_{bS}^{Ma}$ , and 2.4 Hz magnitude  
845  $M_{2.4}^{Ma}$ ) relative to  $M_{W,spec}^{Ma}$  for events with multiple amplitude measurements ( $A_0$  - spectral plateau  
846 amplitude;  $A_P, A_S$  - time domain peak P- and S-wave amplitudes at 0.2 – 0.5 Hz;  $A_{2.4}$ - resonance  
847 amplitude at 2 - 3 Hz in either time or spectral domain).

848

849 **Figure 4. Marsquake magnitudes relative to spectral magnitude,  $M_{W,spec}^{Ma}$ .** Body-wave  
850 magnitudes (a)  $m_b^{Ma}$  and (b)  $m_{bS}^{Ma}$  for low-frequency events (*LF, BB*), and 2.4Hz magnitudes (c)  
851  $M_{2.4,pick}^{Ma}$  and (d)  $M_{2.4,spec}^{Ma}$  for high-frequency events (*HF*) relative to spectral magnitude,  $M_{W,spec}^{Ma}$ ,  
852 which has been used as a calibration reference (and considered to scale with moment  
853 magnitude,  $M_W$ ). Markersize scales with event SNR. The calibration achieves good agreement  
854 across the different scales with standard deviations of  $\sigma = 0.3$  for  $m_b^{Ma}, m_{bS}^{Ma}$ , and of  $\sigma = 0.2$  for  
855  $M_{2.4,pick}^{Ma}$  and  $M_{2.4,spec}^{Ma}$ . The *HF* outlier in (c) is produced by S0490a .

856

857 **Figure 5. Magnitude and distance distribution of marsquakes in the InSight catalog.** Plot  
858 shows all low-frequency (*LF*), broadband (*BB*), high-frequency (*HF*), very high-frequency (*VF*) and  
859 2.4Hz resonance (*2.4Hz*) events. The preferred magnitude is  $M_W^{\text{Ma}} = M_{W,\text{spec},\text{LF}}^{\text{Ma}}$  for *LF* and *BB*  
860 events, to  $M_W^{\text{Ma}} = M_{W,\text{spec},\text{HF}}^{\text{Ma}}$  for *HF* events, and to  $M_W^{\text{Ma}} = M_{2.4,\text{spec}}^{\text{Ma}}$  for *VF* and *2.4Hz* resonance  
861 events. Distances are derived from phase picks (InSight Marsquake Service, 2021), waveform  
862 envelope alignment (Giardini *et al.*, 2020), and a simple crustal model (van Driel *et al.*, 2021),  
863 respectively. Markersize scales with event SNR. Error bars show estimated magnitude and  
864 distance uncertainties. Both distances and magnitudes for the most distant events are uncertain.

865

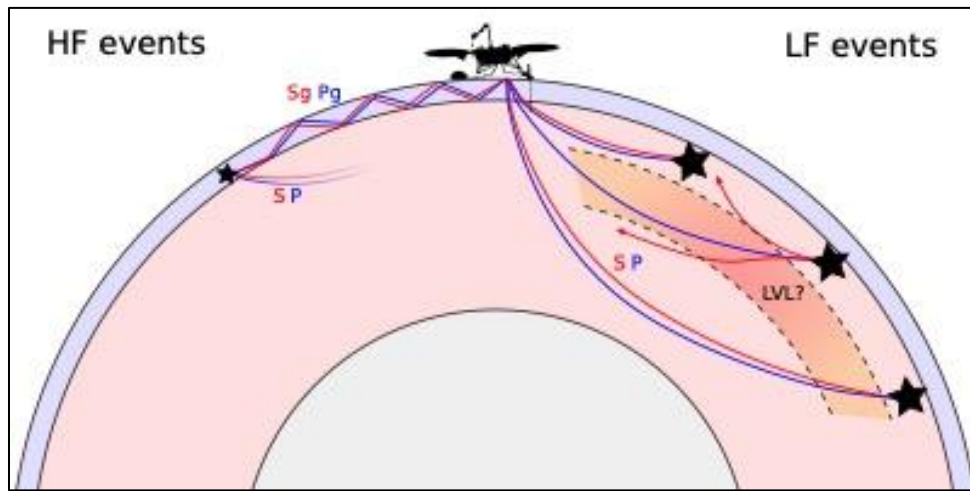
866 **Figure 6. Comparison with magnitude scales on Earth.** Comparison of (a)  $m_b^{\text{Ma}}$  and (b)  $m_{bS}^{\text{Ma}}$   
867 with the body-wave broadband magnitude, *mB* (Gutenberg, 1945a,b) for P- and S-waves on Earth  
868 for all *LF* and *BB* events in the InSight v.5 catalog. Although developed for teleseismic waves at 2 -  
869 20 s period on Earth, we are applying the *mB* relations here to Mars for  $A_P$  and  $A_S$  at 2 - 6 s period.  
870 The good agreement of magnitudes on Mars and Earth suggests a similar attenuation of body-  
871 waves at long periods and teleseismic distances.

872



873 **Figures**

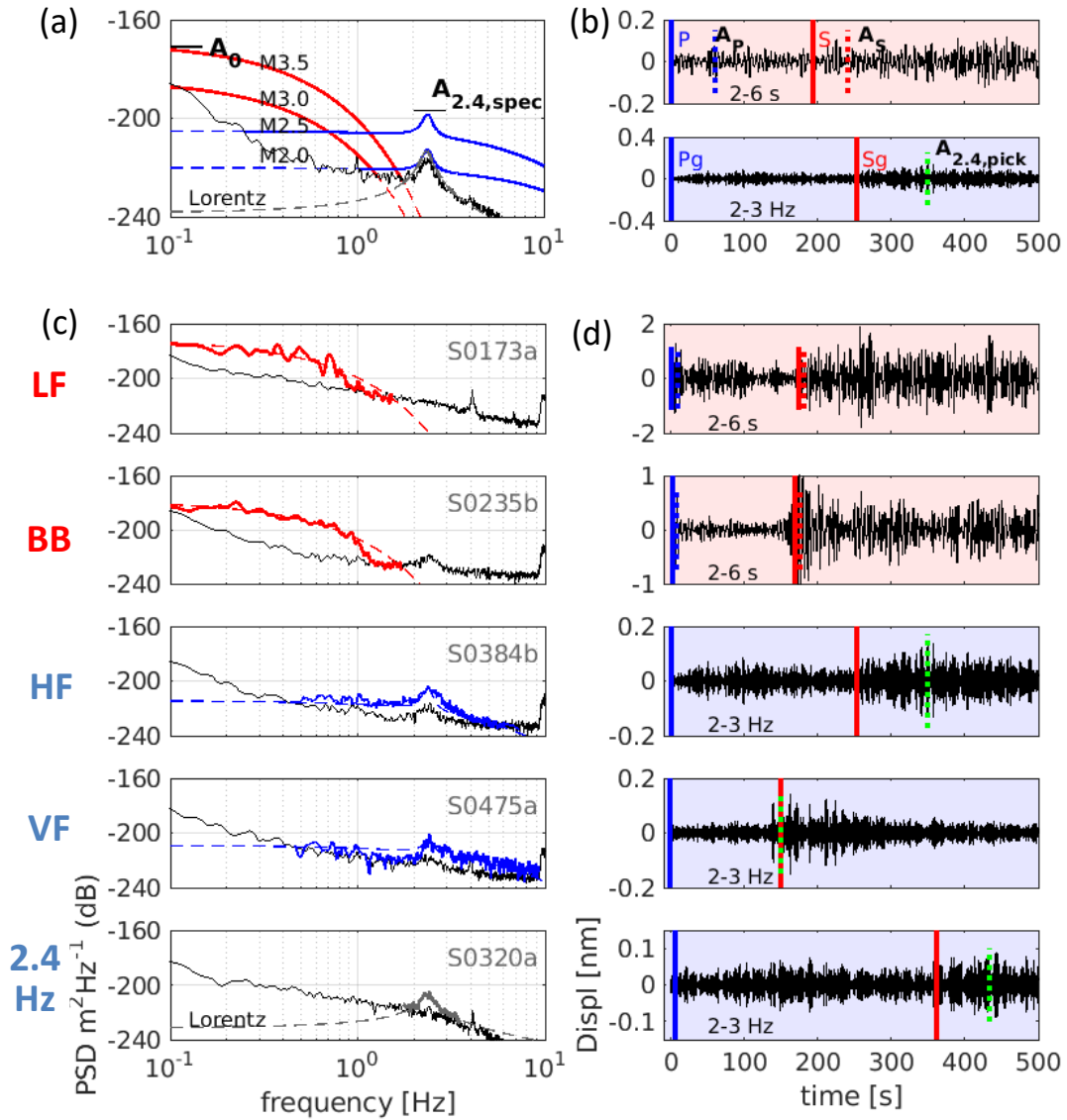
874



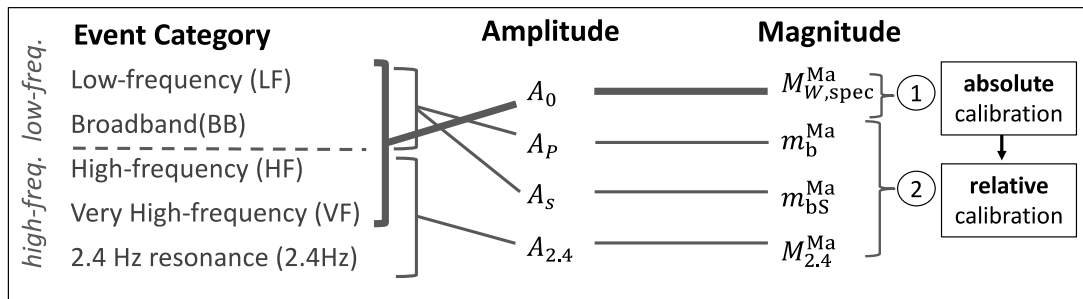
875

876

877 **Figure 1. Seismic wave propagation on Mars.** The current interpretation of seismic signals on  
878 Mars is that events in the high-frequency event family (*HF*, *VF*) excite guided waves in the crust or  
879 in a shallow layer, while events in the low-frequency family (*LF*, *BB*) are located below the Moho;  
880 these mantle waves are observed at long periods due to attenuation. A low-velocity layer (LVL)  
881 could potentially explain the observed distant-dependent variation of S-wave amplitudes.  
882 Modified after Giardini *et al.* (2020).



883  
884 **Figure 2. Amplitude computation from marsquake spectra and waveforms.** (a) Theoretical  
885 spectral shape of power spectral density (PSD) displacement spectra for events of the low-  
886 frequency (*LF*, *BB*; red) and high-frequency (*HF*, *VF*; blue) event families for various magnitudes.  
887 Black line shows typical background noise. (b) Filtered displacement waveforms (vertical  
888 component). Spectral amplitudes  $A_0$  and  $A_{2.4, \text{spec}}$  in (a) are determined from the long-period  
889 plateau of the event displacement spectra and from a Lorentz curve fitted to the 2.4 Hz resonance  
890 peak, respectively. Peak displacement amplitudes  $A_p$  and  $A_s$  in (b) are determined from the  
891 filtered (2 - 6 s, top) displacement waveforms in the time window of the P- or S-wave arrivals. Note  
892 that  $A_s$  is actually picked on the horizontals, while we only show vertical components for the sake  
893 of simplicity.  $A_{2.4, \text{pick}}$  in (b) is determined from the peak amplitude of the 2-3 Hz filtered  
894 displacement waveform (bottom). Subplots in (c) and (d) show example spectra and waveforms  
895 (vertical components) of representative marsquakes of each event category: *LF* - low-frequency,  
896 *BB* - broadband, *HF* - high-frequency, *VF* - very high-frequency, and *2.4Hz* - 2.4Hz ambient  
897 resonance event.



898

899

900

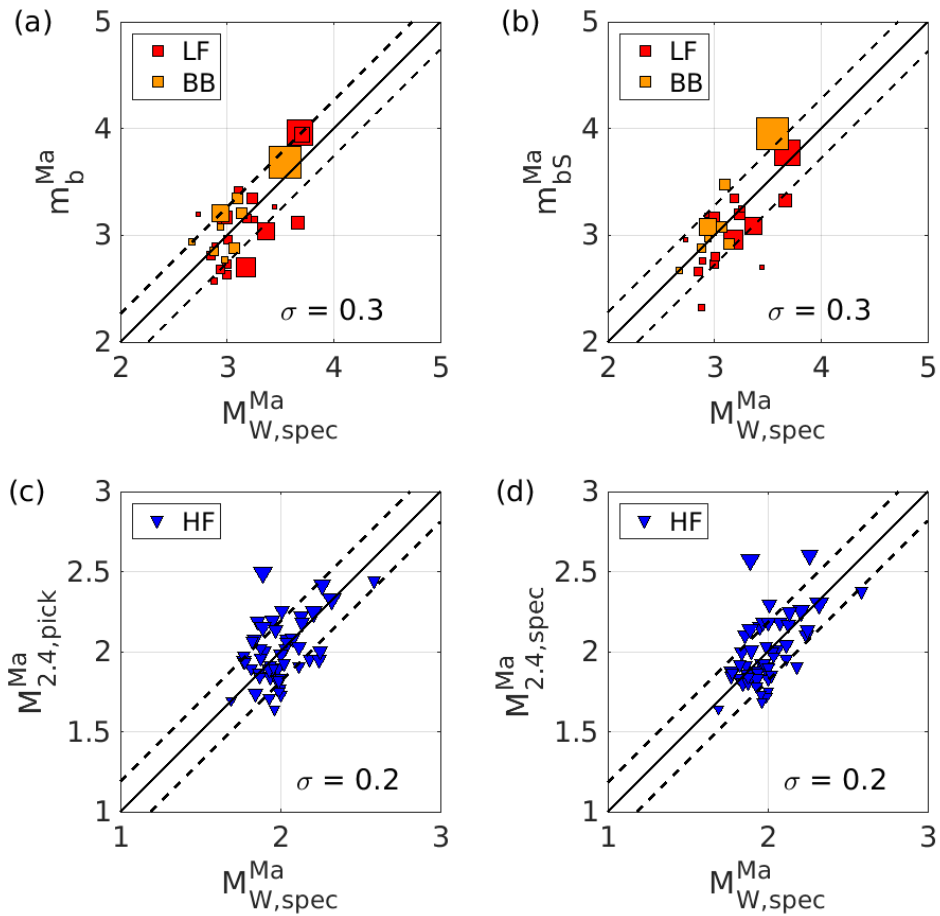
901

902

903

904

**Figure 3. Magnitude calibration for marsquakes.** First, we calibrate the spectral magnitude  $M_{W,spec}^{Ma}$  from synthetic waveforms and theoretical considerations (see main text). Then we calibrate the other magnitude scales (body-wave magnitudes  $m_b^{Ma}$  and  $m_{bS}^{Ma}$ , and 2.4 Hz magnitude  $M_{2.4}^{Ma}$ ) relative to  $M_{W,spec}^{Ma}$  for events with multiple amplitude measurements ( $A_0$  - spectral plateau amplitude;  $A_P$ ,  $A_S$  - time domain peak P- and S-wave amplitudes at 0.2 – 0.5 Hz;  $A_{2.4}$  - resonance amplitude at 2 - 3 Hz in either time or spectral domain).



906

907

908

909

910

911

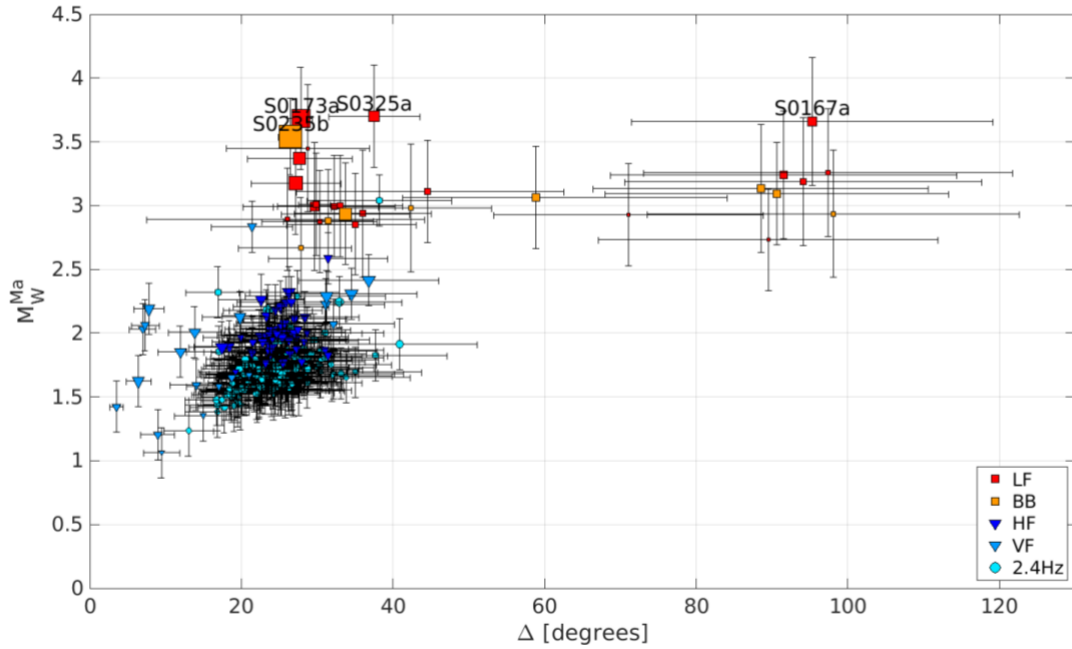
912

913

914

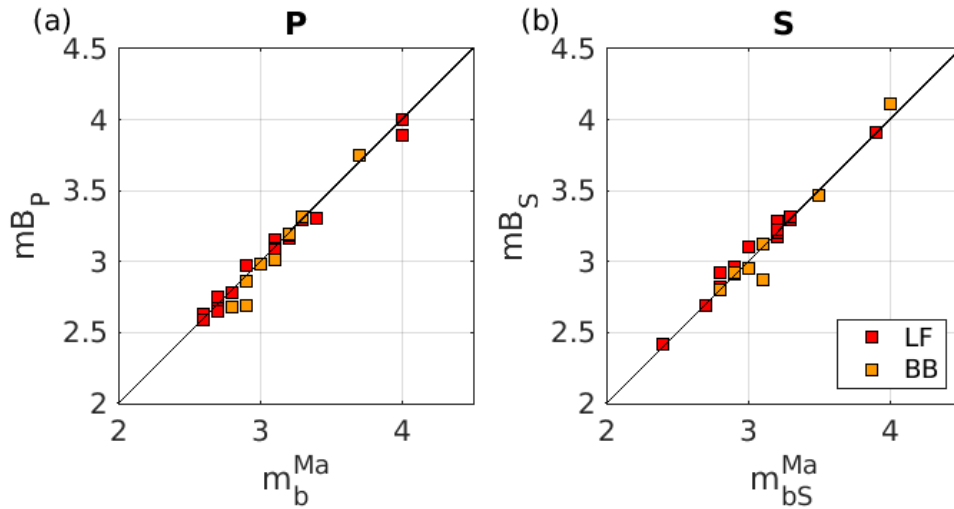
915

**Figure 4. Marsquake magnitudes relative to spectral magnitude,  $M_{W,spec}^{Ma}$ .** Body-wave magnitudes (a)  $m_b^{Ma}$  and (b)  $m_{bS}^{Ma}$  for low-frequency events (*LF*, *BB*), and 2.4Hz magnitudes (c)  $M_{2.4,pick}^{Ma}$  and (d)  $M_{2.4,spec}^{Ma}$  for high-frequency events (*HF*) relative to spectral magnitude,  $M_{W,spec}^{Ma}$  which has been used as a calibration reference (and considered to scale with moment magnitude,  $M_W$ ). Markersize scales with event SNR. The calibration achieves good agreement across the different scales with standard deviations of  $\sigma = 0.3$  for  $m_b^{Ma}$ ,  $m_{bS}^{Ma}$ , and of  $\sigma = 0.2$  for  $M_{2.4,pick}^{Ma}$  and  $M_{2.4,spec}^{Ma}$ . The *HF* outlier in (c) is produced by S0490a.



916  
 917  
 918  
 919  
 920  
 921  
 922  
 923  
 924

**Figure 5. Magnitude and distance distribution of marsquakes in the InSight catalog.** Plot shows all low-frequency (*LF*), broadband (*BB*), high-frequency (*HF*), very high-frequency (*VF*) and 2.4Hz resonance (*2.4Hz*) events. The preferred magnitude is  $M_W^{\text{Ma}} = M_{W,\text{spec},\text{LF}}^{\text{Ma}}$  for *LF* and *BB* events, to  $M_W^{\text{Ma}} = M_{W,\text{spec},\text{HF}}^{\text{Ma}}$  for *HF* events, and to  $M_W^{\text{Ma}} = M_{2.4,\text{spec}}^{\text{Ma}}$  for *VF* and *2.4Hz* resonance events. Distances are derived from phase picks (InSight Marsquake Service, 2021), waveform envelope alignment (Giardini *et al.*, 2020), and a simple crustal model (van Driel *et al.*, 2021), respectively. Marker size scales with event SNR. Error bars show estimated magnitude and distance uncertainties. Both distances and magnitudes for the most distant events are uncertain.



925  
 926  
 927  
 928  
 929  
 930  
 931

**Figure 6. Comparison with magnitude scales on Earth.** Comparison of (a)  $m_b^{Ma}$  and (b)  $m_{bS}^{Ma}$  with the body-wave broadband magnitude,  $mB$  (Gutenberg, 1945a,b) for P- and S-waves on Earth for all *LF* and *BB* events in the InSight v.5 catalog. Although developed for teleseismic waves at 2 - 20 s period on Earth, we are applying the  $mB$  relations here to Mars for  $A_P$  and  $A_S$  at 2 - 6 s period. The good agreement of magnitudes on Mars and Earth suggests a similar attenuation of body-waves at long periods and teleseismic distances.